Redox properties of birnessite from a defect perspective

Haowei Peng[a,1], Ian G. McKendry[b], Ran Ding[b], Akila C. Thenuwara[b], Qing Kang[b], Samantha L. Shumlas[b], Daniel R. Strongin[b], Michael J. Zdilla[b], and John P. Perdew[a,b,1]

[a]Department of Physics, Temple University, Philadelphia, PA 19122; and [b]Department of Chemistry, Temple University, Philadelphia, PA 19122

Birnessite, a layered-structure MnO_2, is an earth-abundant functional material with potential for various energy and environmental applications, such as water oxidation. An important feature of birnessite is the existence of Mn(III) within the MnO_2 layers, accompanied by interlayer charge-neutralizing cations. Using first-principles calculations, we reveal the nature of Mn(III) in birnessite with the concept of the small polaron, a special kind of point defect. Further taking into account the effect of the spatial distribution of Mn(III), we propose a theoretical model to explain the structure–performance dependence of birnessite as an oxygen evolution catalyst. We find an internal potential step which leads to the easy switching of the oxidation state between Mn(III) and Mn(IV) that is critical for enhancing the catalytic activity of birnessite. Finally, we conduct a series of comparative experiments which support our model.

birnessite MnO_2 | small polaron | catalysis | water oxidation

Photoelectrochemical (PEC) splitting of water into H_2 and O_2 (artificial photosynthesis) provides an attractive way to harvest solar energy. The process consists of the oxygen evolution reaction (OER) and the hydrogen evolution reaction (HER), both of which are facilitated with catalysts in practice. Currently, one of the biggest challenges is to develop a cheap and efficient catalyst for the former reaction with a low overpotential, which is still needed to overcome the kinetic barriers (already lowered by the catalyst) along the path from reactants to products. Birnessite, similar to the oxygen-evolving complex in Photosystem II for photosynthesis in regard to the coexistence of Mn(III) (nominal Mn^{3+}) and Mn(IV) (nominal Mn^{4+}) within its structure (1–3), has already shown a moderate catalytic performance with the overpotentials reported from 0.6 V to 0.8 V (4–8).

Birnessite has the general formula $M_xMnO_2 \cdot 1.5(H_2O)$, composed of layers of edge-sharing MnO_6 octahedra as shown in Fig. 1 for the hexagonal phase, and an interlayer of randomly distributed water molecules and metal (M) cations (like K^+, Na^+, and Ca^{2+}). With the charge balanced by the interlayer cations, some of the Mn cations within the MnO_2 layer are reduced from Mn(IV) to Mn(III). The coexistence of Mn(IV) and Mn(III), and further the "balanced equilibrium" or low energy barrier between them, has been suspected to be a critical factor for its catalytic activity (1). The importance of the high-spin Mn(III), through its e_g^1 electronic configuration, has been realized in other manganese oxides for OER catalysis (2, 9) and also follows the design principle of Suntivich et al. (10) that a near-unity e_g occupancy may imply good OER catalytic activity. This easy switching of the oxidation state is also a typical behavior for the transition metal cation undergoing back and forth changes between several oxidation states in OER catalysts during the water oxidation cycle (11–13). OER catalysts like Co- and Ni-doped hematite (12) and cobalt oxides (13), as well as birnessite, operate best in alkaline conditions with a high concentration of OH^-, where the following reaction occurs:

$$4OH^- \rightarrow O_2 + 2H_2O + 4e^-. \qquad [1]$$
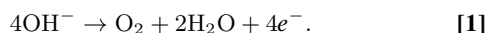
The oxygen evolution cycle involves intermediates where the surface oxygen site is taken by OH, O, OOH, and vacancy species sequentially (equations 1, 2, 4, and 5 in ref. 13). With the occupant changing from OH to O and then to OOH, the oxidation state of the related transition metal cations indeed undergoes an increase and then a decrease by one according to first-principles calculations (12, 13).

However, the existence of Mn(III) does not tell the whole story (2). The activity of birnessite as an OER catalyst still shows a puzzling dependence on structural properties such as the crystal phases, chemical composition, and morphology. Moderate activity for the OER has been experimentally shown for hexagonal birnessites, while the more crystalline form, triclinic birnessite, exhibits no activity for this reaction regardless of the same coexistence of Mn(IV) and Mn(III) within the MnO_2 layers. A much higher activity was found in a highly disordered birnessite-like phase than in the original less-disordered one (3). Focusing on the composition of Mn(III), the authors of ref. 8 observed that some but not all samples with a lower manganese average oxidation state (AOS) were more active for water oxidation. [A lower Mn AOS in birnessite indicates a higher content of Mn(III).] To understand the chemistry behind all these puzzling observations, one must understand the detailed mechanism of Mn oxidation state switching as mentioned above. In this work, we treat the switching between Mn(IV) and Mn(III) as a defect problem, contending it to be the formation and release of an electron small polaron. We propose a theoretical model based on our first-principles computation and further test it via confirming experiments. This model suggests that the oxidation-state switching of Mn in birnessite is facilitated by a potential step along the c axis, induced by an excess of Mn(III) (together with intercalated cations) in the surface layer, which makes it easier for an electron

Significance

We propose, and preliminarily confirm with experiments, a theoretical model to understand various structure–performance dependences of layered-structure birnessite as an oxygen evolution reaction (OER) catalyst. Besides the well-accepted importance of Mn(III), we emphasize the critical importance of a nonuniform distribution of Mn(III) to OER catalytic activity. Such a distribution contributes to the reduction of the overpotential by building an internal potential step. We further propose the small polaron as a common concept to link the fields of oxygen evolution catalysis and Li-ion batteries, suggesting a promising candidate space for oxygen evolution reaction catalysts.

APPLIED PHYSICAL SCIENCES
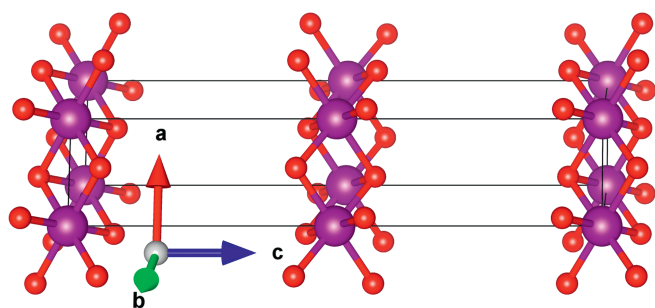
Fig. 1. Crystal structure of hexagonal birnessite MnO_2 (red, oxygen; purple, manganese), without the randomly distributed water molecules and metal cations between the layers for clarity.

to transfer back and forth between Mn ions in the surface and next layers. Our model sheds light on the above-mentioned puzzling structure–performance dependence and further suggests "modulation doping" as a general approach to functionalize layered materials.

Results and Discussion

Birnessite has a complicated structure, with the hydrated cations randomly distributed between the MnO_2 layers, as well as with structural defects (14) within the layer. The role of water molecules is mainly as a structure stabilizer (15), removal of which causes little change to the electronic structure according to a recent computation (16). Hence, we choose the pure hexagonal MnO_2 to study the intrinsic properties, without cation or water intercalation and with the experimental interlayer spacing. Without loss of generality, we assume a ferromagnetic ordering within the layer and an antiferromagnetic ordering between neighboring layers (17). Using this simplified structure model, we focus on Mn(III) and intercalated K, treating them as point defects or defect complexes with the standard supercell approach (18, 19). A $4 \times 4 \times 1$, two-layer, 96-atom supercell is used for our first-principles calculations. The supercell is repeated periodically in all three dimensions.
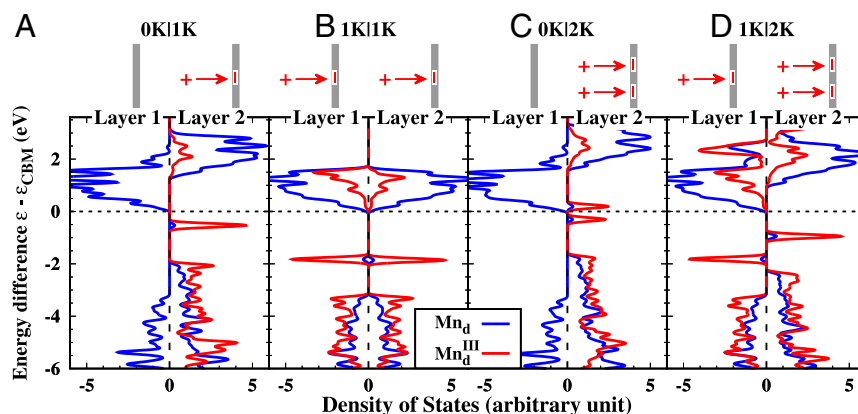
Mn(III) plays a pivotal role for birnessite OER catalytic activity. In some trivalent Mn and Co oxides with an octahedral building block like that in birnessite (9), the localized single e_g electron of the transition metal can form σ bonds with the adsorbates and hence determine the energetics of the intermediates during the OER (10). In operation, usually only a very small portion of Mn sites is actually involved in the reaction, which justifies the defect perspective, and the formation of Mn(III) within the pure MnO_2 matrix can be understood with the concept of the Jahn–Teller electron small polaron: One extra electron, initially located at the conduction band minimum (CBM) and delocalized over the whole crystal, becomes finally well localized (small) around one Mn site with a strong Jahn–Teller local distortion and with the oxidation state of this specific Mn decreasing by one. The energy difference between the final and initial states defines the self-trapping energy E_{ST} for the small polaron, and a negative E_{ST} means a stable small-polaron state. The small polaron is a special kind of point defect and can be explored with the well-established generalized Koopmans' condition (GKC) approach (20–23).

Density of states (DOS), the number of one-electron states with energy ϵ per unit energy (and per atom here), is used for analysis. To account for the self-interaction correction, we use the HSE06 hybrid functional, the standard form of which includes $\alpha = 25\%$ of exact exchange for the intermediate range (24). With HSE06, better energies for the CBM and valence band maximum (VBM) can be obtained for the right reason (25). The GKC further requires that the energy cost to remove an elec-

tron from Mn(III), E_{rem}, equates to minus the eigenvalue of the polaronic electron state, e_{es} (22), all at the fixed nuclear positions of the polaron-containing supercell; here removal is to the CBM of the pristine material. Defining the non-Koopmans energy, $\Delta_{nK} = E_{rem} + e_{es}$, the GKC is $\Delta_{nK} = 0$. To achieve the GKC, we tune the mixing parameter $\alpha = 0.22$ in HSE06 as shown in Fig. 2A. We stick to this α value instead of $\alpha = 0.225$ from interpolation, since 0.02 eV is already well below a typical error bar of the supercell approach. The so-calculated self-trapping energy for an Mn(III) electron small polaron in the pure layered MnO_2 is -0.43 eV. It is negative, indicating that the octahedrally coordinated Mn(IV) in the MnO_2 matrix intrinsically tends to be reduced to Mn(III), given an extra electron. This agrees with the chemical trend previously found in Mn(II) oxides, where the octahedrally coordinated Mn(II) tends to form a hole small polaron, being stable also as an Mn(III) (22, 26). Fig. 2A, *Inset*, showing the squared wavefunction for the small-polaron state, illustrates the degree of localization and the e_g (d_{z^2}) characteristics of the polaronic state. Accounting for the Jahn–Teller distortion, the two axial Mn–O bonds of the distorted octahedron
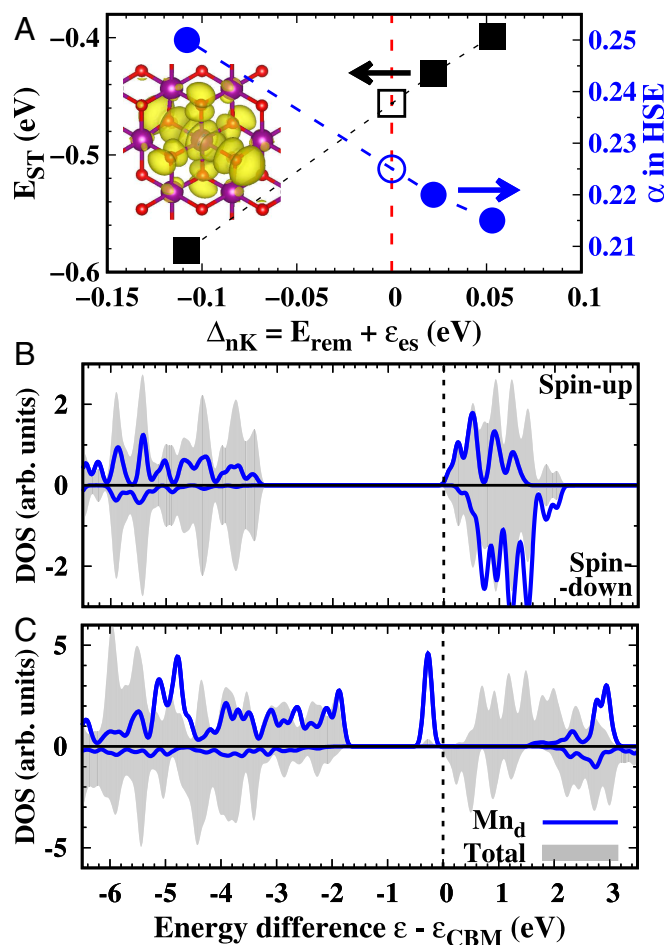
Fig. 2. (A) The self-trapping energy and the mixing parameter α of HSE06 as functions of the non-Koopmans energy Δ_{nK}, with solid symbols for the calculated data points, open symbols for the values under the generalized Koopmans' condition from interpolation, and *Inset* for the squared wavefunction for the small-polaron state. (B and C) The spin-resolved density of states per atom in (B) pristine MnO_2 and (C) MnO_2 with an Mn(III) small polaron, where the shaded area shows the total density of states, the blue curve shows the Mn-d states projected on the site where the small polaron forms, and the energy zero is set to the conduction band minimum energy of each supercell (ignoring the polaronic gap state).

Fig. 3. (*A–D*) Schematic illustration for the structure models (*Upper*) and calculated layer-resolved density of states (*Lower*) for four scenarios: (*A*) zero K associated to layer 1 and one K associated to layer 2 (0K|1K), (*B*) 1K|1K, (*C*) 0K|2K, and (*D*) 1K|2K. The gray bar denotes an MnO$_2$ layer, "+ → |" denotes a K$^+$–Mn(III) or K$^+$–e$^-$ pair, and the energy zero is set to the local conduction band minimum in layer 1 (ignoring the polaronic gap states) to highlight the energy splitting between the conduction band edges of the two layers.

are elongated by about 13%. A small polaron usually results in a low electrical conductivity due to the small-polaron hopping conduction, and our calculation helps to explain the extremely low electrical conductivity of birnessite MnO$_2$ nanowires reported recently (27).

In Fig. 2 *B* and *C*, we compare the spin-resolved DOS for the pristine MnO$_2$ and MnO$_2$ with an Mn(III) polaron. The pristine MnO$_2$ has a band gap of 3.3 eV, with the VBM mainly O-*p*–like and the CBM mainly Mn(IV)-*d*–like with the e_g symmetry [a feature also reproduced by a GGA+U calculation with U around 3 eV on the Mn-*d* orbital (28), but not by semilocal functionals (14)]. The three Mn-*d* electrons of the Mn(IV) ions take the $t_2^3 e_g^0$ configuration within the majority spin channel. When a polaron forms, the configuration changes to $t_2^3 e_g^1$, with the e_g^1 polaronic state located within the band gap. The formation of an Mn(III) small polaron dramatically modifies both the local DOS on the Mn(III) site and the total DOS of the whole crystal. Except for the polaronic peak, the Mn(III)-*d* states are pushed upward in energy as a whole by the enhanced Coulomb repulsion arising from the increased *d*-shell occupancy. Ignoring the polaronic gap state, a big splitting of the conduction band edges between the two spins is also observed. With the interlayer antiferromagnetic ordering, the conduction band edges in the spin-up and spin-down channels are composed of mainly the Mn(IV)-*d* e_g states from the Mn(III)-containing layer and from the other layer of the two-layer supercell, respectively. Therefore, the big spin splitting actually reflects a big potential step between the two MnO$_2$ layers, which arises from the Coulomb repulsion introduced by the extra electron (and its periodic images). The Mn(III)-containing layer has a higher potential (i.e., potential energy of an electron), and we will revisit this later.

To mimic the real samples, we insert metal atoms between the MnO$_2$ layers (with potassium as a prototype), which supply the electrons required to form Mn(III) within the MnO$_2$ layers. We first insert one potassium into the supercell, labeling this scenario "0K|1K" (denoting zero potassium associated to the first layer, layer 1, and one potassium to layer 2) in Fig. 3. The single potassium doping in our two-layer supercell leads to two effects. First the Mn(III) small polaron forms as before, with the needed electron from K (and K becomes K$^+$). The calculated self-trapping energy is −0.38 eV, close to that of the free small polaron. Second, the K–Mn(III), or more appropriately the K$^+$–e$^-$ pair, forms an electrical dipole and therefore induces a local dipole field, raising up the potential of the Mn(III)-containing MnO$_2$ layer. Fig. 3*A* shows the layer-resolved DOS, where the DOS from layers 1 and 2 is plotted with negative and positive

values, respectively. From this plot, one can identify an energy splitting as large as 1.5 eV between the conduction band edges of the two layers (also ignoring the polaronic gap state), larger than that in the case of a free small polaron.

Since the potential step arises from K–Mn(III) pairs, it depends directly on their spatial distribution, and we can use this to tune the electronic structure. As a demonstration, we performed calculations for another three scenarios: 1K|1K (one K–Mn(III) pair for each layer), 0K|2K (zero for layer 1 and two for layer 2), and 1K|2K (one for layer 1 and two for layer 2). The layer-resolved DOSs for all four scenarios are compared in Fig. 3. In scenario 1K|1K, the energy splitting between the conduction band edges zeroes out because the potentials of the two layers are balanced now; the polaronic states located within the original band gap define a new valence band maximum and a new band gap about 2.0 eV, resembling the electronic structure of the triclinic phase with higher K concentration (KMn$_4$O$_8$) from a recent calculation (16). Because of the suitable band gap, this electronic structure has been proposed for PEC water splitting (16), but it may suffer from a weak optical absorption and a low hole mobility. The spatial distribution being more unbalanced in scenario 0K|2K, the energy splitting between the conduction band edges is enhanced. The polaronic state from layer 2 becomes comparable in energy with the CBM defined by the Mn(IV)-d_{e_g} orbitals in layer 1. In this situation, the generalized Janak's theorem (25) suggests that the Mn(III) polaron becomes less stable or metastable, with little or no energy barrier for the transfer of an electron from Mn(III) in layer 2 to layer 1, and the Mn valence increasing from 3 toward 4. In fact, our scenario 0K|2K calculation had to be constrained to prevent this transfer. (The total electron spin per unit cell was constrained.) Finally, in scenario 1K|2K, the energy splitting between the conduction band edges becomes almost the same as that in scenario 0K|1K. To make the potential step self-evident, we plotted in Fig. 4 the *ab*-plane averaged electrostatic potential in layer 2 referenced to the minimum of that in layer 1, for each scenario, between the two layers. We can see that the energy splitting between the conduction band edges of the two layers is strongly correlated to the potential step between the two layers. While our calculation omits intercalated water, we believe that the potential step would survive in at least some distributions of water-molecule positions and orientations.

The OER catalytic activity of hexagonal birnessite is expected to occur on the surface, where there is a higher concentration of Mn(III). We argue that a surface electronic structure similar to scenario 0K|2K should be primarily responsible for the
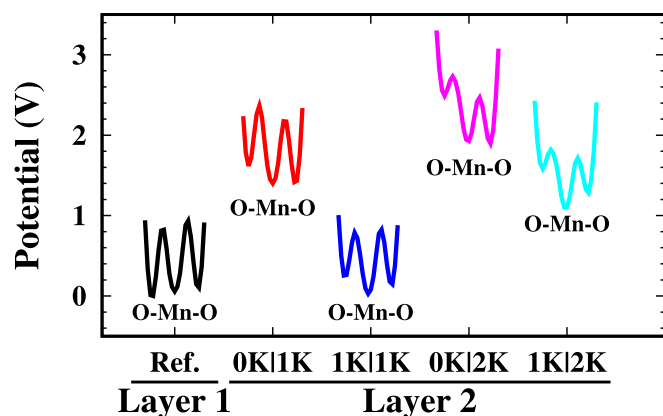
Fig. 4. Calculated *ab*-plane averaged electrostatic potential in layer 2 referenced to the minimum of that in layer 1, for each scenario. The positions of the O-, Mn-, and O-atomic layer within each MnO_2 layer are schematically labeled.

experimentally observed OER catalytic activity of the hexagonal birnessite. The well-crystallized triclinic birnessite, with more evenly distributed cation intercalation and the associated Mn(III), is similar to scenario 1K|1K (16), where Mn(III) is too stable to be an active site for OER catalysis. By contrast, in scenario 0K|2K the Mn(III) and Mn(IV) compete with each other, enabling the Mn cation to adapt its oxidation state to different intermediates during the OER cycle, as other OER catalysts do (11–13). This scenario is in analogy to modulation-doped superlattice structures: Here we modify a subsystem of the layered materials which quantum mechanically connects with the rest. Mn(III) being the representative species here, we tentatively conclude that not only the existence of Mn(III) (9), but also its nonuniform distribution along the *c* direction, is important to enhancing the OER catalytic performance of birnessite. The high OER catalytic activity recently reported in the so-called "activated MnO_x" is very likely due to this mechanism, where the nanosized domain contains an outer-shell disordered birnessite with a higher concentration of Mn(III) than the inner original birnessite phase, as schematically shown in figure 18 of ref. 3.

We further designed two series of comparative experiments to test our theoretical model. Our theoretical model requires a nonuniform distribution of Mn(III) along the *c* direction; hence the less defective triclinic phase and the monolayer nanosheet should be inactive, even with a high Mn(III) content. Such a nonuniform distribution is not possible in the former because of its high crystallization quality or in the latter due to its 2D nature. Fig. 5*A* compares the measured polarization curve (current density vs. overpotential) for the hexagonal, triclinic, and monolayer birnnesite samples. Indeed, consistent with our theoretical predictions, both the triclinic bulk phase and the monolayer nanosheet are not active, while this specific hexagonal bulk sample shows a moderate overpotential around 0.8 V. In particular, the monolayer birnessite does not work for OER catalysis, as predicted by our computation and confirmed by our experiment, in contrast to what one might expect considering the much higher surface-to-volume ratio.

Focusing on the hexagonal phase, we prepared a series of Mn(III)-enriched birnessite samples, with well-controlled structure, phase, and morphology. To achieve this, we started with a single, low-Mn(III)–content birnessite sample, split this sample into separate aliquots, and partially reduced each sample, using a substoichiometric amount of aqueous sodium dithionite ($Na_2S_2O_4$). The dithionite ion reduces Mn(IV) to Mn(III), based on the Mn AOS determined using surface analysis by X-ray photoelectron spectroscopy (XPS) and bulk analysis using

a titration method (*Materials and Methods*). In Fig. 6 we compare XPS for the samples with the highest and lowest AOS, and the enhancement of Mn(III) intensities is shown. The difference between the surface and bulk Mn AOS characterizes the nonuniform distribution of Mn(III) along the *c* direction near the surface. As shown in Fig. 5*B*, the surface Mn AOS decreases faster than the bulk one, which is due to a much higher contact probability with the dissolved $S_2O_4^{2-}$ for the surface (top layers) of the particle. Considering these experimental details, our theoretical model would predict that as the total concentration of Mn(III) increases from zero, the sample should be inactive at the beginning, and then sharply becomes active when the concentration of Mn(III) reaches a critical point where a large enough bulk/surface Mn AOS difference develops. Fig. 5*B* shows the normalized oxygen production as a function of the Mn(III) content. Indeed, the samples are almost inactive with Mn(III)/Mn below 12%, and we see a sharp increase with Mn(III)/Mn between 15% and 20%. In scenario 0K|2K, layer 1 (as presumably the bulk) has an Mn AOS of 4.000, while layer 2, consisting of 2 Mn(III) plus 14 Mn(IV), has an Mn AOS of 3.875. Hence, a difference between the bulk and surface AOS around 0.125 is required to make the polaronic defect states of Mn(III) comparable to the global CBM in energy. In the sample with 20% Mn(III), where the sample becomes active with the current experimental setting, we found a difference between the bulk AOS and surface AOS about 0.14. The experiments are consistent with our theoretical model, both qualitatively and semi-quantitatively.

In the current study, the potential step and the existence of Mn(III) are both controlled by the spatial distribution of the intercalated cations, but they can also be tuned separately. For example, the proposed structural defect complex (30) including an Mn vacancy within the layer and an Mn cation near the layer can form a strong local dipole, and a potential step (or a strong potential fluctuation) can develop via a nonuniform distribution of these defects. Then a metastable Mn(III) small polaron will form in the higher-potential surface layers or region, with an easy switching of the oxidation state. To some extent, the
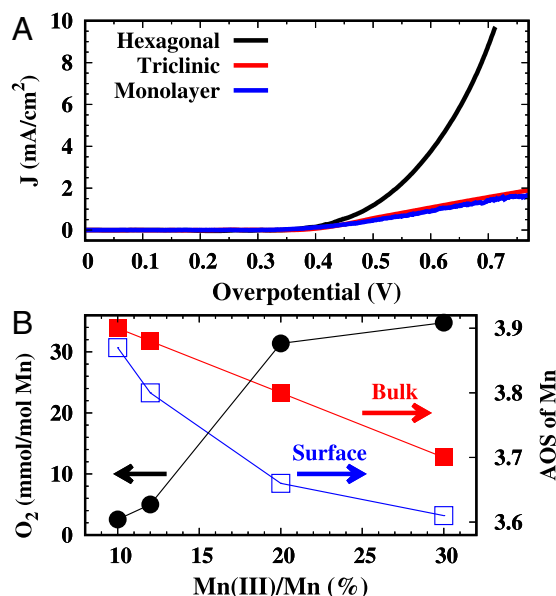
Fig. 5. (*A*) The measured polarization curves, current density *J* as a function of overpotential, in the hexagonal and triclinic birnessite bulk samples and the birnessite monolayer sample. (*B*) The normalized oxygen evolution (left *y* axis), and the AOS of Mn for the whole bulk and surface (right *y* axis), as functions of the bulk Mn(III) composition.
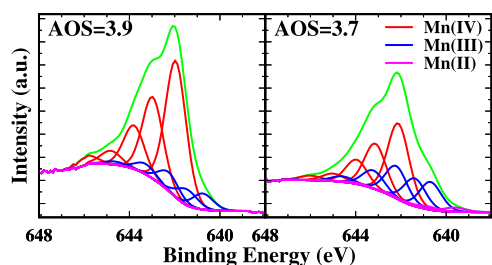
Fig. 6. Mn $2p_{3/2}$ XPS surface analysis of birnessite samples with fittings (29). (*Left*) Synthesized high-AOS birnessite; (*Right*) low-AOS birnessite after sodium dithionite treatment.

potential step built internally, as shown in Fig. 4, contributes to the reduction of the otherwise much larger external bias (overpotential) required to oxidize water. This highlights modulation doping as a promising approach for the functionalization of layered materials.

Conclusion and Outlook

In conclusion, from a defect physics perspective, we proposed a theoretical model to explain and to predict structure–performance dependence of birnessite MnO_2 for oxygen evolution reaction catalysis. The existence of Mn(III) is explained as a Jahn–Teller electron small polaron, and we emphasize that a nonuniform distribution of the Mn(III) perpendicular to the layer is critical for the oxygen evolution reaction catalysis. The small polaron is an undesired factor for functional materials requiring a high electric mobility, but this work suggests it can be tuned to be useful for catalysis. This line of reasoning also provides a concept to link the efforts in the fields of oxygen evolution catalysis and Li-ion batteries, where all of the cathode materials are small-polaron systems.

Materials and Methods

Computation. The first-principles calculations were performed with the projector-augmented wave method (31) as implemented in the VASP code (version 5.4.1) (32–34). A 96-atom $4 \times 4 \times 1$ supercell was used to simulate the free small polaron as well as the K-bound small polaron. Corrections due to the periodic boundary condition and the supercell size have been added (18, 19). The self-trapping energy of the small polaron was calculated with the GKC method, which requires no empirical parameters (20–22). The GKC determines the mixing parameter α in the hybrid functional HSE06 (24) as 0.22, which was used for all calculations. The energy cutoff for the plane-wave basis is 400 eV, and a $2 \times 2 \times 2$ Γ-centered Monkhorst–Pack k mesh (35) is used for the supercell calculations. The internal coordinates of all supercells are relaxed until the residual atomic force is smaller than 0.03 eV/Å. All of the calculations were done with a bulk geometry, but one would expect that the results from surface simulations should be qualitatively similar since the small-polaron formation and potential step due to the uneven distribution of Mn(III) are not surface sensitive, due to the bulk-like encasement of a surface manganese in an oxygen octahedron.

Sample Preparation. Triclinic birnessite was synthesized by using the method by Shumlas et al. (36). Using deionized and deoxygenated water 0.4 M Mn^{2+} solution and 8 M NaOH were mixed (final volume 500 mL) and cooled to 0 °C. Next the suspension was oxidized by bubbling oxygen through the solution for 5 h. After that, the resulting colloidal suspension was aged at 90 °C for 48 h with constant stirring. The resulting product was vacuum filtered and washed multiple times with deionized water.

The hexagonal birnessite sample with the lowest Mn(III) content in Fig. 5*B* was prepared at first via thermal decomposition with a Sentry 2.0 digital temperature controller. $KMnO_4$ powder was pyrolyzed in air for 20 h at 200 °C with heating and cooling rates at 1 °C/min. After decomposition, the mixture was washed by distilled water until the filtrate was colorless. The resulting powder was dried in air and then stored under ambient condition. For birnessite with a higher Mn(III) content, 0.01/0.05/0.1 mmol sodium dithionite solution (20 mL) was added to 10 mmol solution (100 mL) of the low-Mn(III) birnessite, stirred for 1 h, filtrated and washed, and dried

in air. In such a way, the surface receives the most contact with the reductant (sodium dithionite), having higher Mn(III) content than the bulk overall.

The exfoliation of hexagonal birnessite follows this procedure: First, a proton exchange step was carried out where originally present K^+ ions were exchanged by protons by stirring hexagonal birnessite in 0.1 M HNO_3 for 2 d. Next, proton-exchanged hexagonal birnessite was treated with tetra-n-butylammonium hydroxide (TBA^+OH^-; Aldrich Chemical Co., 40 wt% in H_2O) and stirred for 10 d. Unexfoliated material was separated by centrifugation at $1,610 \times g$ for 15 min. After that, the resulting suspension was centrifuged at $8,765 \times g$ for 15 min, and then the sediment was collected and washed with water and ethanol to remove any residual TBAOH. The purified birnessite nanosheets were redispersed in water.

Electrochemical Characterization. The electrochemical analysis was conducted in 1 M KOH (pH ~ 14), using a CHI 660E potentiostat operating in a standard three-electrode configuration at ambient temperature (22 ± 2 °C). Glassy carbon (GC) electrodes (3 mm diameter from CH Instruments) were used as working electrodes. Before electrochemical experiments, the GC electrodes were polished using 1 μm, 0.3 μm, and 0.05 μm alumina powder, respectively, and sonicated in deionized water to clean the electrode surfaces. All of the potentials were measured with respect to a calomel reference electrode (CH Instruments) and Pt wire was used as the counter electrode. The working electrode was prepared by drop casting 5 μL of catalyst ink suspension on the GC electrode (loading 0.28 mg/cm^2). Ink solutions were prepared as follows: Four milligrams of catalyst and 4 mg of carbon (VulcanXC-72) were added to 1 mL isopropanol and 35 μL of Nafion solution (5% in alcohol; Ion Power Inc.), and the resulting mixture was sonicated for at least 30 min to form the catalyst ink. All polarization curves in Fig. 5*A* were recorded at a scan rate of 10 mV/s.

Oxygen Evolution Experiments. Evolved oxygen was measured and recorded via a HACH LD101 Optical Dissolved Oxygen Probe. In general, 25 mg or 50 mg birnessite was stirred in a 15-mL suspension of deionized water (purged with argon for at least 3 h) in a 25-mL filter flask under a nitrogen blanket. A total of 5 mL of argon-purged cerium ammonium nitrate (CAN; 0.4 M, 2 mmol) was added to the suspension via a 10-mL syringe. Induction period measurements were taken every 10 s. All data points were normalized by sample manganese content and zeroed to an initial minimum oxygen concentration.

Determination of Mn Content. To determine total Mn content, 0.50 g of birnessite was dissolved in hydroxylamine hydrochloride (0.5 M, 20 mL) and diluted to 250 mL. Mn content was then determined by analysis of an aliquot of the diluted solution by inductively coupled plasma optical emission spectrometry.

Average Oxidation State of Mn. An oxalic acid–permanganate back titration was used to determine the bulk AOS. First, Mn content was determined as above. Second, a 0.50-g sample of birnessite was completely dissolved in 5 mL of 0.48 M oxalic acid and 5.00 mL H_2SO_4 to reduce all Mn species to Mn(II). The excess oxalate was determined by back titration at 80 °C with a $KMnO_4$ (0.025 M) solution. AOS was calculated according to both the titration result and the total amount of Mn.

XPS for the Surface Mn AOS. X-ray photoelectron spectra (XPS) of dry samples were collected using monochromatic Al K_α X-rays (148.7 eV) generated from a rotating anode and with a high-resolution 300-mm mean radius hemispherical electrostatic analyzer. The base pressure of the analysis chamber was maintained at 10^{-9} Torr. Survey scans were collected using a fixed pass energy of 300 eV and narrow scans were collected using a fixed pass energy of 150 eV. Data collected for the Mn $2p_{3/2}$ spectral region were peak fitted using Casa XPS software. To fit the Mn $2p_{3/2}$ region, the procedure by Nesbit and Banerjee (29) was used that takes into account the multiplet structure resulting from the presence of unpaired valence electrons in the $3d$ orbitals of manganese in the birnessite sample.

1. Birkner N, et al. (2013) Energetic basis of catalytic activity of layered nanophase calcium manganese oxides for water oxidation. *Proc Natl Acad Sci USA* 110:8801–8806.
2. Robinson DM, et al. (2013) Photochemical water oxidation by crystalline polymorphs of manganese oxides: Structural requirements for catalysis. *J Am Chem Soc* 135:3494–3501.
3. Huynh M, Shi C, Billinge SJL, Nocera DG (2015) Nature of activated manganese oxide for oxygen evolution. *J Am Chem Soc* 137:14887–14904.
4. Takashima T, Hashimoto K, Nakamura R (2012) Inhibition of charge disproportionation of MnO_2 electrocatalysts for efficient water oxidation under neutral conditions. *J Am Chem Soc* 134:18153–18156.
5. Indra A, et al. (2013) Active mixed-valent MnOx water oxidation catalysts through partial oxidation (corrosion) of nanostructured MnO particles. *Angew Chem Int Ed* 52:13206–13210.
6. Frey CE, Wiechen M, Kurz P (2014) Water-oxidation catalysis by synthetic manganese oxides–systematic variations of the calcium birnessite theme. *Dalton Trans* 43:4370–4379.
7. Meng Y, et al. (2014) Structure-property relationship of bifunctional MnO_2 nanostructures: Highly efficient, ultra-stable electrochemical water oxidation and oxygen reduction reaction catalysts identified in alkaline media. *J Am Chem Soc* 136:11452–11464.
8. McKendry IG, Kondaveeti SK, Shumlas SL, Strongin DR, Zdilla MJ (2015) Decoration of the layered manganese oxide birnessite with Mn(II/III) gives a new water oxidation catalyst with fifty-fold turnover number enhancement. *Dalton Trans* 44:12981–12984.
9. Maitra U, Naidu BS, Govindaraj A, Rao CNR (2013) Importance of trivalency and the e_g^1 configuration in the photocatalytic oxidation of water by Mn and Co oxides. *Proc Natl Acad Sci USA* 110:11704–11707.
10. Suntivich J, May KJ, Gasteiger HA, Goodenough JB, Shao-horn Y (2011) A perovskite oxide optimized for molecular orbital principles. *Science* 334:1383–1385.
11. Fabbri E, et al. (2014) Developments and perspectives of oxide-based catalysts for the oxygen evolution reaction. *Catal Sci Technol* 4:3800–3821.
12. Liao P, Keith JA, Carter EA (2012) Water oxidation on pure and doped hematite (0001) surfaces: Prediction of Co and Ni as effective dopants for electrocatalysis. *J Am Chem Soc* 134:13296–13309.
13. Bajdich M, García-Mota M, Vojvodic A, Nørskov JK, Bell AT (2013) Theoretical investigation of the activity of cobalt oxides for the electrochemical oxidation of water. *J Am Chem Soc* 135:13521–13530.
14. Kwon KD, Refson K, Sposito G (2008) Defect-induced photoconductivity in layered manganese oxides: A density functional theory study. *Phys Rev Lett* 100:146601.
15. Matsui H, Ju J, Odaira T, Toyota N (2009) Two-dimensionally confined water in between MnO_2 layers of Na-birnessite. *J Phys Soc Jpn* 78:074801.
16. Lucht KP, Mendoza-Cortes JL (2015) Birnessite: A layered manganese oxide to capture sunlight for water-splitting catalysis. *J Phys Chem C* 119:22838–22846.
17. Kan M, Zhou J, Sun Q, Kawazoe Y, Jena P (2013) The intrinsic ferromagnetism in a MnO_2 monolayer. *J Phys Chem Lett* 4:3382–3386.
18. Lany S, Zunger A (2008) Assessment of correction methods for the band-gap problem and for finite-size effects in supercell defect calculations: Case studies for ZnO and GaAs. *Phys Rev B* 78:235104.
19. Kumagai Y, Oba F (2014) Electrostatics-based finite-size corrections for first-principles point defect calculations. *Phys Rev B* 89:195205.
20. Lany S, Zunger A (2009) Polaronic hole localization and multiple hole binding of acceptors in oxide wide-gap semiconductors. *Phys Rev B* 80:085202.
21. Lany S (2011) Predicting polaronic defect states by means of generalized Koopmans density functional calculations. *Phys Status Solidi B* 248:1052–1060.
22. Peng H, Lany S (2012) Semiconducting transition-metal oxides based on d^5 cations: Theory for MnO and Fe_2O_3. *Phys Rev B* 85:201202.
23. Peng H, Ndione PF, Ginley DS, Zakutayev A, Lany S (2015) Design of semiconducting tetrahedral $Mn_{1-x}Zn_xO$ alloys and their application to solar water splitting. *Phys Rev X* 5:021016.
24. Krukau AV, Vydrov OA, Izmaylov AF, Scuseria GE (2006) Influence of the exchange screening parameter on the performance of screened hybrid functionals. *J Chem Phys* 125:224106.
25. Perdew JP, et al. (2017) Understanding band gaps of solids in generalized Kohn–Sham theory. *Proc Natl Acad Sci USA* 114:2801–2806.
26. Peng H, et al. (2013) Li-doped Cr_2MnO_4: A new *p*-type transparent conducting oxide by computational materials design. *Adv Funct Mater* 23:5267–5276.
27. Le M, et al. (2015) In situ electrical conductivity of Li_xMnO_2 nanowires as a function of *x* and size. *Chem Mater* 27:3494–3504.
28. Dudarev SL, Botton GA, Savrasov SY, Humphreys CJ, Sutton AP (1998) Electron-energy-loss spectra and the structural stability of nickel oxide: An LSDA+U study. *Phys Rev B* 57:1505–1509.
29. Nesbitt HW, Banerjee D (1998) Interpretation of XPS Mn(2*p*) spectra of Mn oxyhydroxides and constraints on the mechanism of MnO_2 precipitation. *Am Mineral* 83:305–315.
30. Lanson B, Drits VA, Silvester E, Manceau A (2000) Structure of H-exchanged hexagonal birnessite and its mechanism of formation from Na-rich monoclinic buserite at low pH. *Am Mineral* 85:826–838.
31. Blöchl PE (1994) Projector augmented-wave method. *Phys Rev B* 50:17953.
32. Kresse G, Hafner J (1994) Ab initio molecular-dynamics simulation of the liquid-metal–amorphous-semiconductor transition in germanium. *Phys Rev B Condens Matter* 49:14251–14269.
33. Kresse G, Furthmüller J (1996) Efficient iterative schemes for ab initio total-energy calculations using a plane-wave basis set. *Phys Rev B Condens Matter* 54:11169–11186.
34. Kresse G, Joubert D (1999) From ultrasoft pseudopotentials to the projector augmented-wave method. *Phys Rev B* 59:1758–1775.
35. Monkhorst H, Pack J (1976) Special points for Brillouin-zone integrations. *Phys Rev B* 13:5188–5192.
36. Shumlas SL, et al. (2016) Oxidation of arsenite to arsenate on birnessite in the presence of light. *Geochem Trans* 17:5.

Peng et al.